Peer reviewed version

Link to published version (if available):

Link to publication record in Explore Bristol Research
PDF-document

University of Bristol - Explore Bristol Research
General rights

Wall shear stress exposure time: A Lagrangian measure of near-wall stagnation and concentration in cardiovascular flows

Amirhossein Arzani[1]   Alberto M. Gambaruto[2]   Guoning Chen[3]

Shawn C. Shadden[1]

[1]Department of Mechanical Engineering, University of California Berkeley, Berkeley, CA, United States
[2]Department of Mechanical Engineering, University of Bristol, Bristol, UK
[3]Department of Computer Science, University of Houston, Houston, TX, United States

Correspondence:
Amirhossein Arzani
University of California
2167 Etcheverry Hall
Berkeley, California 94720-1740
Email: arzani@berkeley.edu

Abstract

Near-wall transport is of utmost importance in connecting blood flow mechanics with cardiovascular disease progression. The near-wall region is the interface for biologic and pathophysiologic processes such as thrombosis and atherosclerosis. Most computational and experimental investigations of blood flow implicitly or explicitly seek to quantify hemodynamics at the vessel wall (or lumen surface), with wall shear stress (WSS) quantities being the most common descriptors. Most WSS measures are meant to quantify the frictional force of blood flow on the vessel lumen. However, WSS also provides an approximation to the near-wall blood flow velocity. We herein leverage this fact to compute a wall shear stress exposure time (WSSET) measure that is derived from Lagrangian processing of the WSS vector field. We compare WSSET against the more common relative residence time (RRT) measure, as well as a WSS divergence measure, in several applications where hemodynamics are known to be important to disease progression. Because these measures seek to quantify near-wall transport and because near-wall transport is important in several cardiovascular pathologies, surface concentration computed from a continuum transport model is used as a reference. The results show that compared to RRT, WSSET is able to better approximate the locations of near-wall stagnation and concentration build-up of chemical species, providing an increase in correlation to surface concentration from 0.51 to 0.79 in the examples considered. Because WSSET considers integrated transport behavior, it can be more

1

suitable in regions of complex hemodynamics that are traditionally difficult to quantify, yet encountered in many disease scenarios.

1 Introduction

Biomechanical interactions between blood flow and the vessel wall are central to the initiation and progression of most cardiovascular diseases. Indeed, the majority of computational and experimental investigations into blood flow seek to understand how local flow mechanics relates to disease progression in or on the vessel wall. Blood flow conditions in diseased vessels are usually spatially and temporally complex and are challenging to characterize [51, 50], even without reference to the coupled biochemical or biophysical processes driving disease progression. Nonetheless, the role of blood flow mechanics in the "near-wall" region is of utmost importance since this is where such couplings are most profound. In the near-wall region, blood flow serves to impart mechanical stresses on the vessel wall, as well as regulate the local transport of reactive material between the tissue and fluid domains. It is this latter mechanism that motivates the work presented herein.

A compelling scenario involving the interaction between blood flow and the vessel wall is atherosclerosis, which is a leading cause of death worldwide. Atherosclerosis occurs mainly in locations of disturbed blood flow patterns [9, 47]. The local transport of several substances near and at the vessel wall are known to influence atherosclerosis progression [56]. For example, previous studies have looked into transport of low density lipoproteins (LDL) [17, 20, 30, 14], high density lipoproteins (HDL) [40, 24], oxygen [16, 27], nitric oxide (NO) [45, 35], monocytes [12, 14], and adenine triphosphate ATP and adenine diphosphate ADP [13, 15, 8] as important mass transport processes involved in atherosclerosis.

Intravascular thrombosis is another compelling pathology associated with most cardiovascular diseases where near-wall transport becomes important [7, 25]. The trajectories of individual platelets and the accumulation and residence time of chemical solutes including ADP, thrombin, and various blood factors control clot formation. These solutes, and especially in activated form, are generated at the vessel wall or from bound platelets. Complex hemodynamics and flow stagnation are often associated with prothrombotic conditions. For example, intraluminal thrombus in abdominal aortic aneurysm (AAA) [57, 54] complicates disease progression, and is thought to be strongly coupled to flow stagnation and recirculation. The chaotic flow field in AAAs [3] leads to complex WSS distributions [4] and interesting near-wall flow structures [1]. Thrombosis in the left ventricle [49], aortic dissection [41], stented arteries [28], and flow diverter treated cerebral aneurysms [43] represent other applications of complex transport potentially affecting local thrombosis.

Near-wall transport can either be (i) explicitly modeled for a specific transport problem, or (ii) inferred from appropriate hemodynamics measures. For explicit modeling, most computational investigations of intravascular transport have relied on continuum models that solve the advection-diffusion equations in the blood flow domain. However, due to the high Schmidt numbers (Sc) in most arterial flows, thin concentration boundary layers are typically formed next to the wall where most interesting biological processes occur [19]. The thin concentration boundary layer thickness causes numerical difficulties in resolving the near-wall dynamics [23], which is precisely the region of greatest interest. Hansen and Shadden [23] recently proposed a continuum surface transport model to study mass transport in the thin concentration boundary layer next to the wall. This model is based on the idea that the core flow minimally influences the mass transport in the concentration boundary layer in high Sc flows, and thus surface transport PDEs can be derived in terms of the WSS vector field.

On the other hand, to report, compare and more generally evaluate hemodynamic processes it is important to develop simple measures that effectively quantify physiologically-relevant aspects of near-wall transport. Flow stagnation is one important aspect of transport, which has been widely regarded as an event promoting atherogenic and thrombogenic processes. In order to quantify near-wall stagnation, particle tracking techniques have been used to define near-wall residence time [37]. While the Lagrangian nature of this measure is desirable for capturing emergent behavior of the flow, a very high resolution of particles is often needed to accurately sample the near-wall region. A more readily obtained measure is relative residence time (RRT), which is defined as the inverse of time average WSS (TAWSS) vector magnitude [26, 32]. The relevance of this measure could be explained as follows. As discussed in [23, 1], the WSS vector can be scaled to obtain the near-wall fluid velocity, and because displacements of fluid in the concentration boundary layer are small over each cardiac cycle, the time-averaged WSS vector field dominates transport. Therefore, in regions of low TAWSS vector magnitude (high RRT) the near-wall species are displaced to smaller extent, implying higher near-wall stagnation. However, because RRT is an instantaneous Eulerian measure, it cannot as effectively provide information about the concentration or origin of near-wall species when compared to a Lagrangian measure. This can be valuable information, since high near-wall stagnation and concentration are both essential for effective atherogenic or thrombogenic processes to occur.

In this paper, we present a WSS exposure time (WSSET) measure that is computed from Lagrangian tracking of surface-born tracers, which can account for stagnation (low flow) and species redistribution. It has the advantage of being a Lagrangian-based measure that accounts for the emergent role of transport, but has significantly less computational cost compared to explicitly solving a full transport problem. We compare WSSET with RRT in different vascular pathologies. To this end, image-based models of aortic aneurysm, carotid bifurcation, cerebral aneurysm, and coronary aneurysm are used. WSS divergence is also computed and its relevance to near-wall transport is discussed. Because a key importance of altered hemodynamics is the effect on chemical species distribution near the lumen, these measures were compared with surface concentration fields obtained from the solution of a complete 3D advection-diffusion transport problem. We demonstrate that WSSET is able to better approximate the locations of near-wall stagnation and concentration build-up of chemical species. This improvement comes at an increased computational cost when compared to RRT, however this cost is far below that needed to explicitly solve the full 3D transport problem. To further demonstrate the relevance of the WSSET measure and to characterize the near-wall flow topology, stable and unstable manifolds of fixed points in the TAWSS vector field are computed and related to WSSET fields. These manifolds help explain observed WSSET and surface concentration patterns. Namely, unstable manifolds determine the regions where concentration build-up occurs, and stable manifolds can mark the basins of attraction, e.g., the regions where near-wall species become attracted to particular TAWSS fixed points or TAWSS unstable manifolds. Because these manifolds can be computed directly from the topology of the TAWSS vector field, they can help predict surface transport patterns without having to actually perform the Lagrangian surface transport calculations required to compute WSSET.

2 Methods

2.1 Computational fluid dynamics (CFD)

Six patient-specific AAA models were used in this study and WSS data was obtained from computational fluid dynamics (CFD) simulations using the software package SimVascular (simvascular.org), as described in [5]. The models were constructed from magnetic resonance imaging and started from the supra celiac aorta and continued to the iliac arteries, including the major branch arteries. Inflow and outflow boundary conditions were tuned to match measured, patient-specific flow rates and blood pressures. A stabilized finite element method was used to solve the Navier-Stokes equations, using linear tetrahedral elements. The mesh edge size next to the wall was 200 μm, and the time step divided the cardiac cycle into 1000 time steps. Using SimVascular, two carotid artery models were constructed from computed tomography angiography. Linear tetrahedral elements were used with a global edge size of 400 μm and a boundary layer meshing with next to wall edge size of 50 μm. The mean common carotid volumetric flow rate used in a previous study [31] was assigned as inlet boundary condition for both patients. Resistance boundary conditions were used at the outlets to divide 70% of the flow rate to the internal carotid artery and 30% to the external carotid artery. The time step was chosen to divide the cardiac cycle (T = 0.88 s) into 5000 time steps. A cerebral aneurysm model used in a previous study [22] was remeshed with a higher mesh resolution (next to wall edge size of 100 μm). The same boundary conditions and parameters used in [22] were specified. A typical volumetric waveform was used at the inlet with the flow rate scaled according to the inlet cross section area. Zero pressure gradient was applied at the outlet. The time step divided the cardiac (T = 0.85 s) cycle to 100 time steps. Similarly, a coronary aneurysm model (Kawasaki disease) used in a previous study [48] was remeshed with a higher resolution (next to wall edge size of 60 μm in the aneurysm branch). The same boundary conditions and parameters were used for the flow solution (this model and simulation parameters were obtained from vascularmodel.com). A typical aortic waveform was prescribed at the inlet, and a circuit analogy lumped parameter network was coupled to the outlets to model coronary pressure and flow. The simulation time step was 1 ms. Rigid wall and Newtonian blood rheology were assumed in all simulations. The cerebral aneurysm simulation was done in OpenFOAM (finite volume method), and all the other simulations were carried out in SimVascular (finite element method). Figure 1 shows the full computational models, and the highlighted region shows the region of interest where flow conditions were analyzed using the WSSET, RRT and WSS divergence measures.

2.2 Near-wall stagnation

In this section, the WSS measures used to quantify near-wall stagnation are defined. The WSS vector field ($\boldsymbol{\tau}$) is computed as the tangential component of traction on the wall. Relative residence time (RRT), a traditional measure used in characterization of near-wall stagnation, is defined as

$$\text{RRT} = \frac{1}{\|\frac{1}{T}\int_0^T \boldsymbol{\tau}\,dt\|} = \frac{1}{\|\overline{\boldsymbol{\tau}}\|}\ , \tag{1}$$

where T is the cardiac cycle duration, and $\overline{\boldsymbol{\tau}} = \frac{1}{T}\int_0^T \boldsymbol{\tau}dt$ is the TAWSS vector. Note that this definition is the same as the more common form written in terms of oscillatory shear index (OSI)

$$\text{RRT} = \frac{1}{(1-2\cdot\text{OSI})\int_0^T \|\boldsymbol{\tau}\|dt} \ , \tag{2}$$
$$\text{OSI} = \frac{1}{2}\left(1 - \frac{\|\overline{\boldsymbol{\tau}}\|}{\int_0^T \|\boldsymbol{\tau}\|dt}\right) \ .$$

The form in Eq. (1) provides a clearer correspondence to TAWSS vectors and near-wall transport. We also compute time averaged WSS divergence (WSSdiv)

$$\text{WSSdiv} = \frac{1}{T}\int_0^T \nabla \cdot \boldsymbol{\tau}dt \ . \tag{3}$$

Positive WSSdiv represents expansion of WSS vectors, and negative WSSdiv shows contraction, which could exemplify flow impingement and separation, respectively. The relevance of this measure to near-wall flow will be demonstrated.

In this study, a recent method for characterization of near-wall stagnation based on WSS trajectories is used. The near-wall fluid velocity can be represented based on the WSS vector field to first order [21, 34] as

$$\boldsymbol{u}_\pi = \frac{\boldsymbol{\tau}\delta n}{\mu} + O(\delta n^2) \ , \tag{4}$$

where $\boldsymbol{u}_\pi$ is the near-wall tangential velocity evaluated in a small normal to the wall distance δn, and μ is the dynamic viscosity. A mass diffusion coefficient of $D = 1 \times 10^{-5}\frac{cm^2}{s}$ [16] is assumed to estimate the species concentration boundary layer thickness $\delta_c = \delta Sc^{\frac{-1}{3}}$, where δ is the momentum boundary layer thickness, and $Sc = \frac{\nu}{D}$ where ν is blood's kinematic viscosity. A normal to wall distances of $\delta n = 15\mu m$, $0.7\mu m$, $1\mu m$, and $1\mu m$ are chosen in this study, which are within δ_c in the AAA, carotid artery, cerebral aneurysm, and coronary aneurysm models, respectively. The significance of this choice is discussed in our previous study [1].

The methods used in [58, 10] for surface streamline tracing were extended to unsteady surface vector fields to generate WSS pathlines. Trajectories are seeded on the entire surface of the region of interest uniformly and integrated based on the near-wall fluid velocity (Eq. 4). Thus, we consider here the evolution of surface-born species. In order to obtain a uniform initial distribution of surface trajectories, OpenFlipper (www.openflipper.org) was used to remesh the triangular surface mesh to the desired number of vertices while enforcing a uniform distribution of vertices. These vertices were used as the initial location of the surface trajectories. Trajectories were computed using a forward Euler integration with sufficiently small time step. These WSS trajectories were computationally confined to stay on the surface, while they represent the trajectories in a small near-wall distance δn. To confine these trajectories on the curved surface, the computation is conducted within the individual triangular (i.e., linear) elements of the surface, which are locally planar. The coordinate conversion between two neighboring triangles during the numerical integration is achieved via the transformation of the two corresponding local coordinate systems.

In order to quantify near-wall stagnation, WSSET [1] is computed for each triangular surface element as the accumulated amount of time that all the WSS trajectories spend

inside that element, with proper normalizations

$$\text{WSSET}(e) = \frac{1}{\mathcal{T}}\sqrt{\frac{A_m}{A_e}} \sum_{p=1}^{N_t} \int_0^{\mathcal{T}} H_e(p,t)\,\mathrm{d}t \qquad (5)$$

$$H_e = \begin{cases} 1 \text{ if } \boldsymbol{x}_p(t) \in e \\ 0 \text{ if } \boldsymbol{x}_p(t) \notin e \end{cases},$$

where A_e is the area of the surface element, A_m is the average area of all the surface elements, $\mathbf{x}_p(t)$ is the position of the WSS trajectory, H_e is the indicator function for element e, N_t is the total number of trajectories released, and $\mathcal{T}$ is the integration time. An integration time of 100 cardiac cycles ($\mathcal{T} = 100T$) was used for each patient, and the WSS data was assumed periodic to enable trajectory integration for such time scale.

2.3 Advection-diffusion transport

Simulations of chemical concentration fields on surface of each model were computed by solving the 3D advection-diffusion equation to provide a comparison of the wall-bounded WSS measures with the full 3D transport. The advection-diffusion equation can be written as

$$\frac{\partial c}{\partial t} + \boldsymbol{u} \cdot \nabla c = D\nabla^2 c\,, \qquad (6)$$

where c is a non-dimensional concentration, $\boldsymbol{u}$ is the velocity, and D is the same mass diffusivity as above. A Neumann boundary condition of $\frac{\partial c}{\partial n} = 5\,cm^{-1}$ was prescribed at the no-slip wall representing a uniform flux of concentration into the lumen. Zero Dirichlet boundary conditions were used at the inlet and outlets. Homogenous Dirichlet outlet boundary conditions were preferred to homogenous Neumann, due to backflow at the outlets. The outlet boundary was extended based on the available CFD data (between 1 to 3 times the diameter) to ensure minimal influence of the outlet boundary condition and improve convergence. The advection-diffusion equation was solved using the finite element method implemented in the FEniCS package [36]. Second-order tetrahedral elements were used with an edge size of 0.1 cm , 400 μm, 400 μm, and 200 μm in the interior for the AAA, carotid artery, cerebral aneurysm, and coronary aneurysm models, respectively. A boundary layer mesh was generated with next to wall edge size of 6.6 μm, 1.5 μm, 1.6 μm, and 1.6 μm for the AAA, carotid artery, cerebral aneurysm, and coronary aneurysm models, respectively. The velocity field obtained from the CFD simulation was linearly interpolated to the (more highly resolved in the near-wall region) advection-diffusion mesh. The simulations were run for at least 25 cardiac cycles until the surface concentration reached steady state, with very small intra-cycle fluctuations.

2.4 WSS stable/unstable manifolds

We have previously demonstrated emergence of Lagrangian coherent structures (LCS) computed from WSS (WSS LCS) and how they relate to the near-wall transport in AAAs [1]. The WSS LCS were computed by integrating a high resolution of surface tracers and identifying

the distinct material lines formed. These structures match the stable and unstable manifolds of the TAWSS vector in high Schmidt numbers, where $\delta n \sim \delta_c$ is small [1]. Therefore, the TAWSS vector field alone could be used in characterization of near-wall flow topology in such flows, as opposed to the time-dependent WSS vector field (assuming periodicity of the flow field for TAWSS to be sensible). Employing this observation, we use a different method than our previous study [1] to directly compute WSS LCS by computing stable and unstable manifolds of the (steady) TAWSS vector field. A stable and unstable manifold corresponding to a saddle-type fixed point of a vector field are the set of all the trajectories that asymptote to the fixed point in forward and backward time integrations, respectively. The unstable manifold tends to attract nearby trajectories, and the stable manifold tends to repel nearby trajectories in time and therefore these structures are often identified as attracting and repelling LCS, particularly in the context of unsteady vector fields. This direct approach captures all WSS stable and unstable manifolds, whereas our previous method only identified the more prominent ones. Moreover, this approach significantly reduces computational time since it does not require Lagrangian surface transport computation, but is rather based on topological analysis of the TAWSS vector field.

Stable and unstable manifolds of TAWSS fixed points are computed to identify WSS LCS, a template for near-wall transport. The first step in this approach is the detection of the fixed points of the TAWSS vector field, which can be achieved by locating the triangles whose Poincaré indices are non-trivial (i.e., 1 or -1) [55]. Next, the vector field is linearized around the fixed points $\mathbf{x}_0$, i.e., $\overline{\boldsymbol{\tau}}(\mathbf{x}) = \overline{\boldsymbol{\tau}}(\mathbf{x}_0) + J_{\mathbf{x}_0}(\mathbf{x} - \mathbf{x}_0)$, where $J_{\mathbf{x}_0} = \nabla \overline{\boldsymbol{\tau}}(\mathbf{x}_0)$ is the Jacobian of $\overline{\boldsymbol{\tau}}$, from which the two eigenvalues/eigenvectors are computed. The fixed points that are of saddle-type (i.e their two eigenvalues are real and have different signs, and the eigenvectors are real) are identified. These fixed points are perturbed along the positive eigenvector (i.e., corresponding to the positive eigenvalue) in two opposite directions to obtain two initial conditions [22]. The WSS trajectories constructed from these initial conditions in forward time will trace out the unstable manifold. Similarly, perturbation along the negative eigenvector (i.e., corresponding to the negative eigenvalue) direction with backward time integration delineates the stable manifold. The trajectory integration is continued until the trajectory reaches another fixed point (typically a source or sink) or leaves the domain. Figure 2 depicts the procedure for computation of TAWSS manifolds and WSSET.

3 Results

Figure 3 and 4 show contour plots of WSSET, RRT, WSSdiv, and surface concentration for the AAA (P1–P6) and the other (P7–P10) models, respectively. It is observed that some of the features in regions of high WSSET and RRT match. However, a comparison of WSSET and RRT to surface concentration reveals that WSSET features are in better agreement with surface concentration. The agreement between RRT and surface concentration is improved for the simpler geometries, due to the simpler flow topology. In general, regions of high WSSET have high RRT and negative WSSdiv. However, this trend does not occur in all regions. The motivation behind the WSSdiv measure shown in the figures is that regions of negative WSSdiv correspond to converging WSS vectors, which can indicate accumulation of near-wall trajectories in these regions.

Scatter plots of the data are shown for a better comparison of the WSS measures. Figure 5 shows scatter plots of WSSdiv vs. RRT colored based on the WSSET value. This figure shows that high WSSET largely occurs where WSSdiv is negative and RRT is higher than a certain threshold. No apparent correlation was observed between RRT and WSSdiv. The reason for this is that RRT is based on the wall shear stress, which is proportional to the tangential velocity component, while WSSdiv is proportional to near-wall normal velocity [21, 1], thus these measures represent orthogonal velocity components. Figures 6 and 7 show scatter plots of the data comparing RRT and WSSET measures to surface concentration. The rank of the data are plotted in these figures instead of the values. This was chosen due to the nonlinear nature of the WSSET measure, which produces a wide range of values, thereby restricting any linear correlation between the data. Namely, as the integration time becomes higher, more WSS trajectories accumulate near certain fixed points of the TAWSS vector field, contributing to very high WSSET values in the vicinity of these fixed points. These figures demonstrate that WSSET has a strong correlation with surface concentration. Table 1 shows the Spearman's rank correlation coefficient between the WSS measures and surface concentration. WSSET and RRT are both correlated with surface concentration, however the WSSET correlation is stronger. The improvement in the WSSET correlation over RRT is more pronounced in the AAA and cerebral aneurysm models, which have more complex flows. WSSdiv is inversely correlated with surface concentration; however, the correlation is not as strong as the other measures. No correlation is obtained for WSSdiv in the coronary aneurysm case, although as Fig. 4 and 5 demonstrate regions of high surface concentration and WSSET still mostly coincides with negative WSSdiv.

Figures 8 and 9 show the stable and unstable manifolds of the TAWSS vector field colored by red and blue lines, respectively. The vector lengths are normalized for visualization and colored based on their magnitude. Comparison of these figures with Fig. 3 and 4 shows that unstable manifolds of TAWSS lead to high WSSET and high surface concentration in their surroundings. Near-wall trajectories are attracted to unstable manifolds of TAWSS and accumulate around these manifolds producing high WSSET and high surface concentration. In order to quantify the matching between TAWSS unstable manifolds and regions of high WSSET and surface concentration, Table 2 shows the percentage of the unstable manifold length existing in a region greater than the 80th percentile of these measures.

Figure 10 shows an example of how the intersections of stable and unstable manifolds of TAWSS vector divide the surface into different regions. Region I and II are the basins of attraction for the first fixed point (F1). WSS trajectories starting in these regions are attracted to this fixed point. Similarly, region III and IV are the basins of attraction for the second fixed point (F2). WSS trajectories starting in region V leave the aneurysm region, therefore region V could be regarded as the basin of attraction for a fixed point in infinity.

3.1   Thrombin transport: a case study

In order to compare our results to an example of a precise biochemical transport mechanism, thrombin transport is considered. The problem involves the initiation phase of thrombin production in the coagulation cascade, similar to previous studies [42, 23]. The presence of tissue factor at the prothrombotic wall turns prothrombin into thrombin. Platelets are ignored, as the initiation phase of thrombin production is only considered. The total concentration of

thrombin (c_{IIa}) and prothrombin (c_{II}) is assumed constant and equal to the prothrombin concentration at the inlet of the domain (C_0). The reactive boundary condition at the wall is written as $D\frac{\partial c_{II}}{\partial n} = -kc_{II}$, where $k = 9.75 \times 10^{-6}\frac{cm}{s}$ is the surface reaction rate [42] and $\mathbf{n}$ is the outward normal vector. Using $c_{IIa} + c_{II} = C_0$, the surface boundary condition for thrombin can be written as

$$D\frac{\partial c_{IIa}}{\partial n} = k(C_0 - c_{IIa}) \, , \tag{7}$$

where $D = 2 \times 10^{-6}\frac{cm^2}{s}$ is set to approximate shear-enhanced diffusivity of thrombin [52]. The advection-diffusion equation with the above surface boundary condition and zero concentration boundary conditions at the inlet and outlet were used to simulate thrombin generation and transport. The above equation is a Robin type boundary condition, as opposed to the Neumann boundary condition previously used at the wall.

Figure 11 shows the thrombin surface concentration normalized by prothrombin concentration at the inlet for the first patient. The value of C_0 was set to 1 in the simulation. Thrombin surface concentration correlation to the WSS measures are also shown in the figure, demonstrating a good correlation between WSSET and thrombin surface concentration. It should be mentioned that for this patient, the WSSET and RRT correlation to surface concentration was reduced 7% and 14% respectively, compared to the previous generic Neumann boundary condition.

4   Discussion

Near-wall transport is of paramount importance in cardiovascular mass transport problems. The reasons for this are two-fold. First, hemodynamics directly affects pathophysiology, such as intimal hyperplasia, atherosclerosis or thrombosis, by controlling the transport of chemical and cellular species near the vessel wall. Second, the high Sc numbers encountered in arterial flows leads to the formation of thin concentration boundary layers next to the wall, which marginalizes the *direct* effect of the core flow on near-wall transport. The explicit modeling and computation of near-wall transport of a chemical species is numerically challenging, however we demonstrated herein that computation of WSSET can be used to quantify and predict the transport of wall-born species.

In this study we have proposed WSSET as a novel measure for quantification of near-wall stagnation and concentration. WSSET quantifies the concentration and amount of time that wall-generated species spend near the wall. Consequently, regions of high WSSET typically exhibit negative WSSdiv and elevated RRT. A comparison of WSS measures to surface concentration shows that WSSET has the best correlation with surface concentration. Namely, WSSET measures concentration residence time, and hence quantifies what is expected to be a driving mechanism for atherogenic or thrombogenic processes. WSS LCS, computed from stable and unstable manifolds of TAWSS vector field saddle points, provide insight on the near-wall flow topology and help explain WSSET distributions. Unstable manifolds of TAWSS attract the trajectories in their basin of attraction, thus trajectories accumulate near these manifolds contributing to high WSSET. Stable manifolds of TAWSS repel their nearby trajectories and mark the boundaries of different basins of attraction.

In the context of the endothelial cells (ECs) lining the vessel wall, such cells are known to sense and respond to their environment by *direct* and *indirect* mechanisms [6]. In the direct mechanism, ECs sense and respond to mechanical forces by converting forces to chemical signals (mechanotransduction) and reorganizing their cytoskeleton to affect gene expression or cell functionality [11]. In the indirect mechanism, agonists in the blood flow interact with ECs to activate various responses [18]. WSS provides a means to quantify both near-wall mechanisms. For the direct mechanism, WSS measures the frictional force per unit area exerted on the ECs. For the indirect mechanism, WSS is a surrogate for the near-wall transport velocity, and WSSET can be used to quantify the potential for indirect mechanisms on EC response.

While solving the 3D advection-diffusion equation directly quantifies the complete transport of any continuum species, the high computational cost and numerical difficulties involved in accurately resolving the concentration boundary layer makes this approach prohibitively expensive in routine image-based hemodynamics applications. Computation of WSSET is far less computationally expensive, but still able to accurately convey and characterize near-wall transport. Due to the quasi-steady nature of near-wall transport, the TAWSS vector can be used as a steady vector to compute WSSET, producing nearly identical results compared to the unsteady WSS vector field [1]. We note, however, that RRT can be computed from WSS with trivial computational effort and provides good agreement with WSSET and surface concentration in relatively simple flow environments–making it a preferred measure in such applications. WSS LCS can be computed with minimal computational time and can provide mechanistic insight not conveyed by WSSET or RRT fields. In this study, various arterial domains were considered to characterize different flow conditions in locations known to influence pathology. The results show that RRT mostly holds in laminar scenarios, however WSSET is predictive over a broader range of flow conditions.

While flow stagnation affects intravascular biological processes, it is more broadly the concentration of near-wall species, and perhaps their origin, that is more directly important. For example, Chiu *et al.* [12] have shown that monocyte adhesion to ECs occurs in regions of high near-wall concentration and long residence time. Near-wall species spend more time in regions of low TAWSS due to the smaller near-wall fluid velocity. This near-wall stagnation is captured by both RRT and WSSET measures. However, the WSSET measure is influenced not only by the amount of time that trajectories spend near the wall, but also the concentration of near-wall trajectories and their origin. In relation, the fixed points of TAWSS that have larger basins of attraction will generate higher WSSET in their vicinity (cf. Fig. 10). The stable manifolds of TAWSS show the boundary of these basins of attraction and could be used to estimate how much an attracting fixed point contributes to high WSSET.

OSI [29] is a leading WSS measure that has been widely used to characterize oscillations in the WSS vector field. The main motivation behind this measure is the observation that ECs prefer to align in regions with a well defined TAWSS vector direction and demonstrate inflammatory response in regions with oscillatory WSS. From a transport perspective, the peak value of OSI = 0.5 corresponds to a TAWSS vector with zero magnitude (infinite RRT). Therefore, in these regions no net tangential convective displacement occurs contributing to high near-wall stagnation. On the other hand, in a region with zero OSI the WSS vector does not change its direction, therefore contributing to a potentially larger TAWSS vector magnitude with a typically well defined direction. However, the OSI measure by itself does

not explain transport. OSI only explains amplification or reduction in effective near-wall transport. This observation is similar to concepts of mobility discussed by [39] in a broader context of Eulerian vector field characterization. Regions of low OSI contribute to a more effective near-wall convective tangential transport, whereas high OSI reduces effective transport due to the rapid temporal change in WSS vector. It should be emphasized though that the WSS vector magnitude needs to be considered to quantify near-wall transport. Recently, the prevailing theory that atherosclerosis is positively correlated with OSI has been challenged [44]. A possible explanation for these inconsistencies may be that many experimental studies impose uniform oscillatory flow in simple settings. This can lead to (exaggeratedly) high near-wall stagnation, promoting atherogenic processes. However, in vivo values of OSI are typically more moderate, and in such contexts the correspondence between locations of higher OSI and the accumulation of near-wall species is less direct. Due to the spatially uniform or less complex flows in experimental studies, this phenomena can be overlooked.

In order to compute WSSET, we seeded trajectories uniformly on the surface. These trajectories represent surface-generated near-wall species. Therefore, regions of high WSSET will represent high near-wall concentration of species if the effective flux of species is coming from the lumen into the fluid domain. In correspondence with the Eulerian advection-diffusion equation, this implies that the flux boundary condition at the wall needs to be inward (into the lumen). In cases where the flux boundary condition at the wall is outward (into the vessel wall) and uniform concentration of species exists at the inlet of the domain (e.g. oxygen), opposite relations would be obtained (see the Appendix Sec 6). For instance, at a reattachment or impingement point, a source type fixed point in the WSS vector field can be generated. This source will push wall-generated trajectories away, therefore causing low WSSET in its vicinity. However, if the species are coming from the core flow, high concentration will occur in this region. Therefore, it is important to keep the nature of the transport process in mind when measures such as WSSET or RRT are being studied.

Another important consideration is that WSS and the flux boundary condition at the wall can be interconnected. For example, WSS can affect the permeability of the ECs to certain species, therefore creating a shear-stress-dependent mechanism for the resistance of the surface to mass transfer [53]. WSS can also influence the flux of wall-generated species. For example, high WSS can lead to a higher flux of NO at the vessel wall [45]. These effects could be accounted for in the WSSET approach by releasing tracers at each location proportional to the non-uniform flux. However, such modifications can not be integrated in the RRT measure.

We have ignored the effect of diffusion and normal velocity on the WSSET measure. We have previously investigated these effects and observed that the qualitative behavior of WSSET is minimally changed [1]. Diffusion causes random near-wall trajectories to escape the near-wall region in long integration times, therefore the WSSET is generally reduced. Normal velocity is second order in δn and generally small near the wall; however, it is proportional to WSS divergence [21] :

$$u_n = -\frac{1}{2\mu}\nabla \cdot \boldsymbol{\tau}\, \delta n^2 + O(\delta n^3)\ . \tag{8}$$

Significant negative WSS divergence can cause near-wall trajectories to escape the near-

wall region. The effect of WSS divergence on WSSET can become important in higher Reynolds numbers where the WSS divergence can become very high. In the present study, we only used one cardiac cycle of WSS data and assumed periodicity to generate WSS trajectories, although cycle-to-cycle variations in WSS exist in some cardiovascular flows such as AAAs [46]. However, our aim in this study was to demonstrate the applicability of our approach and comparison to existing methods. In this study, to characterize the near-wall flow topology we computed the stable/unstable manifolds of TAWSS vector. This is based on the observation that the near-wall transport is quasi-steady and the WSS LCS match the TAWSS stable/unstable manfiolds [1]. However, this quasi-steady behavior can break down if the Reynolds and Womersley numbers are sufficiently increased. For example, exercise in AAA patients creates a more complex flow field [2], with higher WSS values [33]. A preliminary investigation of our methods on AAA exercise data showed that the WSS LCS can slightly fluctuate around the stable/unstable manifolds of TAWSS and demonstrate some time dependence behavior (results not shown). Fortunately, in order to characterize the near-wall stagnation, the WSSET measure can still be applied under these flow conditions, since it is a Lagrangian approach. However, the relevance of RRT as an Eulerian measure becomes questionable, since the TAWSS vector no longer indicates effective near-wall transport. Time-averaged measures like RRT always have the risk of being inaccurate if their averaging time does not capture the flow transients. It should be noted that biological processes occur on the order of days/months, therefore multiscale simulations are needed to evaluate such long-term processes. Moreover, inclusion of experimental or clinical data, providing a direct link between WSSET and clinical events would be another topic of future studies. Finally, the Newtonian blood rheology assumption might be questionable. This can potentially affect our results in two different ways. First, the WSS vector field obtained from a Newtonian and non-Newtonian assumption can be different, although these differences have been shown to be small in patient-specific AAAs [38]. Second, variations in viscosity affect the near-wall fluid velocity in Eq. 4. However, these variations only scale the near-wall fluid velocity and will not change the near-wall velocity direction. Therefore, as long as these changes in the magnitude of the near-wall fluid velocity do not violate the quasi-steady transport behavior, WSS LCS will still be identified from stable/unstable manifolds of the TAWSS vector. Consequently, the same near-wall flow topology will persist and the qualitative aspect of WSSET will not be affected.

5 Conclusion

The transport of chemical and cellular species near the vessel wall (or lumen) directly affects the initiation and progression of most cardiovascular diseases. Hence the characterization of near-wall transport is a primary concern in hemodynamics research. Directly tracking an advected species in the blood flow domain to understand near-wall transport, through Lagrangian particle-tracking or solving the Eulerian advection-diffusion equations, is computationally difficult because of the disparate spatial and temporal scales between the bulk flow and near-wall regions in high Sc cardiovascular flows. To resolve this challenge, we proposed WSSET as a Lagrangian measure to quantify near-wall transport. This measure is computed from only the WSS vector field, and thus the resolution of the CFD need only

be sufficient to solve the Navier-Stokes equation, and the tracking of particles is reduced to only a surface flow. Compared to the traditional RRT measure of near-wall transport, the application of WSSET to six AAA, two carotid artery, one cerebral aneurysm, and one coronary aneurysm models demonstrated improved ability to predict high and low species concentrations at the lumen. In addition, computation of WSS LCS from stable and unstable manifolds of saddle fixed points of the TAWSS vector field were shown to be relevant in the characterization of the near-wall flow topology–namely, unstable manifolds of TAWSS lead to elevated WSSET and surface concentration in their vicinity, whereas stable manifolds of the TAWSS were shown to mark basins of attraction. In summary, WSSET is a new hemodynamic parameter solely based on the WSS vector field that can provide a reasonable approximation of near-wall concentration, quantified by 3D continuum transport.

6 Appendix

6.1 Transport to and from the wall

In this section, an analogy between transport into the wall versus transport from the wall is established. In Section 2.3 we considered the problem of continuum transport from the wall into the lumen. However, certain chemicals such as oxygen are transported from the lumen into the wall. Assuming a homogenous concentration at the inlet, such problems can be written as

$$\frac{\partial c}{\partial t} + \boldsymbol{u} \cdot \nabla c = D\nabla^2 c \,, \tag{9a}$$

$$c = c_0 \quad \text{Inlet}\,, \tag{9b}$$

$$\frac{\partial c}{\partial n} = -A \quad \text{Wall.} \tag{9c}$$

In order to observe the analogy between this problem and the considerations of Section 2.3, let us introduce a new variable $\widetilde{c} = c_0 - c$. Substituting this into Eq 9 for c and simplifying gives:

$$\frac{\partial \widetilde{c}}{\partial t} + \boldsymbol{u} \cdot \nabla \widetilde{c} = D\nabla^2 \widetilde{c}\,, \tag{10a}$$

$$\widetilde{c} = 0 \quad \text{Inlet}\,, \tag{10b}$$

$$\frac{\partial \widetilde{c}}{\partial n} = A \quad \text{Wall.} \tag{10c}$$

Note that this is the same problem that is solved in Section 2.3. Therefore, referring to the change of the variable introduced, an increase (decrease) in c corresponds to a decrease (increase) in $\widetilde{c}$. Therefore, in the regions where WSSET predicts high concentration, a low concentration is actually obtained if the transport is originated from the lumen and travels into the wall. However, this is not an issue as a direct analogy can be established between the two cases. A few remarks follow.

Remark 1. The value of A will have different physical meanings in the two problems, and therefore its value will be different. However, this difference simply shifts the concentration values uniformly.

Remark 2. The above analogy is physically correct as long as $\widetilde{c} \leq c_0$. The issue arises in the negative flux boundary condition introduced in Eq 9. The negative flux boundary condition $\frac{\partial c}{\partial n} = -A$ will be physically wrong if c becomes zero near the wall, and this will lead to erroneous negative values for c at the wall. The requirement for c to be positive leads to $\widetilde{c} \leq c_0$.

Remark 3. The above issue does not occur if one considers a physically more realistic Robin type boundary condition $\frac{\partial c}{\partial n} = -kc$, where k is a constant. It should be mentioned that the incorporation of a Robin type boundary condition breaks the analogy, although the analogy is expected to hold in some qualitative extent, as demonstrated for thrombin/prothrombin transport (Figure 11). Future work should investigate this claim for other biochemical transports.

Acknowledgements

Funding

Conflict of interest

The authors have no conflict of interest.

References

[1] A. Arzani, A. M. Gambaruto, G. Chen, and S. C. Shadden. Lagrangian wall shear stress structures and near-wall transport in high-Schmidt-number aneurysmal flows. *Journal of Fluid Mechanics*, 790:158–172, 2016.

[2] A. Arzani, A. S. Les, R. L. Dalman, and S. C. Shadden. Effect of exercise on patient specific abdominal aortic aneurysm flow topology and mixing. *International Journal for Numerical Methods in Biomedical Engineering*, 30(2):280–295, 2014.

[3] A. Arzani and S. C. Shadden. Characterization of the transport topology in patient-specific abdominal aortic aneurysm models. *Physics of Fluids*, 24(8):081901, 2012.

[4] A. Arzani and S. C. Shadden. Characterizations and correlations of wall shear stress in aneurysmal flow. *Journal of Biomechanical Engineering*, 138(1):014503, 2016.

[5] A. Arzani, G. Y. Suh, R. L. Dalman, and S. C. Shadden. A longitudinal comparison of hemodynamics and intraluminal thrombus deposition in abdominal aortic aneurysms. *American Journal of Physiology-Heart and Circulatory Physiology*, 307(12):H1786–H1795, 2014.

[6] A. I. Barakat and D. K. Lieu. Differential responsiveness of vascular endothelial cells to different types of fluid mechanical shear stress. *Cell Biochemistry and Biophysics*, 38(3):323–343, 2003.

[7] D. Basmadjian. The effect of flow and mass transport in thrombogenesis. *Annals of Biomedical Engineering*, 18(6):685–709, 1990.

[8] E. Boileau, R. L. T. Bevan, I. Sazonov, M. I. Rees, and P. Nithiarasu. Flow-induced ATP release in patient-specific arterial geometries–a comparative study of computational models. *International Journal for Numerical Methods in Biomedical Engineering*, 29(10):1038–1056, 2013.

[9] C. G. Caro, J. M. Fitz-Gerald, and R. C. Schroter. Arterial wall shear and distribution of early atheroma in man. *Nature*, 223:1159–1161, 1969.

[10] G. Chen, K. Mischaikow, R. S. Laramee, P. Pilarczyk, and E. Zhang. Vector field editing and periodic orbit extraction using morse decomposition. *Visualization and Computer Graphics, IEEE Transactions on*, 13(4):769–785, 2007.

[11] S. Chien. Mechanotransduction and endothelial cell homeostasis: the wisdom of the cell. *American Journal of Physiology-Heart and Circulatory Physiology*, 292(3):H1209–H1224, 2007.

[12] J. J. Chiu, C. N. Chen, P. L. Lee, C. T. Yang, H. S. Chuang, S. Chien, and S. Usami. Analysis of the effect of disturbed flow on monocytic adhesion to endothelial cells. *Journal of Bbiomechanics*, 36(12):1883–1895, 2003.

[13] H. W. Choi, K. W. Ferrara, and A. I. Barakat. Modulation of ATP/ADP concentration at the endothelial surface by shear stress: effect of flow recirculation. *Annals of Biomedical Engineering*, 35(4):505–516, 2007.

[14] M. Cilla, E. Peña, and M. A. Martínez. Mathematical modelling of atheroma plaque formation and development in coronary arteries. *Journal of The Royal Society Interface*, 11(90):20130866, 2013.

[15] A. Comerford, M. J. Plank, and T. David. Endothelial nitric oxide synthase and calcium production in arterial geometries: an integrated fluid mechanics/cell model. *Journal of Biomechanical Engineering*, 130(1):011010, 2008.

[16] G. Coppola and C. Caro. Oxygen mass transfer in a model three-dimensional artery. *Journal of The Royal Society Interface*, 5(26):1067–1075, 2008.

[17] M. Dabagh, P. Jalali, and J. M. Tarbell. The transport of LDL across the deformable arterial wall: the effect of endothelial cell turnover and intimal deformation under hypertension. *American Journal of Physiology-Heart and Circulatory Physiology*, 297(3):H983–H996, 2009.

[18] P. F. Davies. Flow-mediated endothelial mechanotransduction. *Physiological Reviews*, 75(3):519–560, 1995.

[19] C. R. Ethier. Computational modeling of mass transfer and links to atherosclerosis. *Annals of Biomedical Engineering*, 30(4):461–471, 2002.

[20] S. Fazli, E. Shirani, and M. R. Sadeghi. Numerical simulation of LDL mass transfer in a common carotid artery under pulsatile flows. *Journal of Biomechanics*, 44(1):68–76, 2011.

[21] A. M. Gambaruto, D. J. Doorly, and T. Yamaguchi. Wall shear stress and near-wall convective transport: Comparisons with vascular remodelling in a peripheral graft anastomosis. *Journal of Computational Physics*, 229(14):5339–5356, 2010.

[22] A. M. Gambaruto and A. J. João. Flow structures in cerebral aneurysms. *Computers & Fluids*, 65:56–65, 2012.

[23] K. B. Hansen and S. C. Shadden. A reduced-dimensional model for near-wall transport in cardiovascular flows. *Biomechanics and Modeling in Mechanobiology*, 15(3):713–722, 2016.

[24] W. Hao and A. Friedman. The LDL-HDL profile determines the risk of atherosclerosis: a mathematical model. *PloS One*, 9(3):e90497, 2014.

[25] J. J. Hathcock. Flow effects on coagulation and thrombosis. *Arteriosclerosis, Thrombosis, and Vascular Biology*, 26(8):1729–1737, 2006.

[26] H. A. Himburg, D. M. Grzybowski, A. L. Hazel, J. A. LaMack, X. M. Li, and M. H. Friedman. Spatial comparison between wall shear stress measures and porcine arterial endothelial permeability. *American Journal of Physiology-Heart and Circulatory Physiology*, 286(5):H1916–H1922, 2004.

[27] F. Iori, L. Grechy, R. W. Corbett, W. Gedroyc, N. Duncan, C. G. Caro, and P. E. Vincent. The effect of in-plane arterial curvature on blood flow and oxygen transport in arterio-venous fistulae. *Physics of Fluids (1994-present)*, 27(3):031903, 2015.

[28] J. M. Jiménez, V. Prasad, M. D. Yu, C. P. Kampmeyer, A. H. Kaakour, P. J. Wang, S. F. Maloney, N. Wright, I. Johnston, Y. Z. Jiang, and P. F. Davies. Macro- and microscale variables regulate stent haemodynamics, fibrin deposition and thrombomodulin expression. *Journal of The Royal Society Interface*, 11(94):20131079, 2014.

[29] D. N. Ku, D. P. Giddens, C. K. Zarins, and S. Glagov. Pulsatile flow and atherosclerosis in the human carotid bifurcation. positive correlation between plaque location and low oscillating shear stress. *Arteriosclerosis, Thrombosis, and Vascular Biology*, 5(3):293–302, 1985.

[30] J. Lantz and M. Karlsson. Large eddy simulation of LDL surface concentration in a subject specific human aorta. *Journal of Biomechanics*, 45(3):537–542, 2012.

[31] S. W. Lee, L. Antiga, J. D. Spence, and D. A. Steinman. Geometry of the carotid bifurcation predicts its exposure to disturbed flow. *Stroke*, 39(8):2341–2347, 2008.

[32] S. W. Lee, L. Antiga, and D. A. Steinman. Correlations among indicators of disturbed flow at the normal carotid bifurcation. *Journal of Biomechanical Engineering*, 131(6):061013, 2009.

[33] A. S. Les, S. C. Shadden, C. A. Figueroa, J. M. Park, M. M. Tedesco, R. J. Herfkens, R. L. Dalman, and C. A. Taylor. Quantification of hemodynamics in abdominal aortic aneurysms during rest and exercise using magnetic resonance imaging and computational fluid dynamics. *Annals of Biomedical Engineering*, 38:1288–1313, 2010.

[34] M. Lévêque. Les lois de la transmission de chaleur par convection. *Ann Mines*, 13:201–239, 1928.

[35] X. Liu, Y. Fan, X. Y. Xu, and X. Deng. Nitric oxide transport in an axisymmetric stenosis. *Journal of The Royal Society Interface*, 9(75):2468–2478, 2012.

[36] A. Logg, K. A. Mardal, and G. Wells. *Automated solution of differential equations by the finite element method*, volume 84. Springer, Berlin, Heidelberg, 2012.

[37] P. W. Longest and C. Kleinstreuer. Numerical simulation of wall shear stress conditions and platelet localization in realistic end-to-side arterial anastomoses. *Journal of Biomechanical Engineering*, 125(5):671–681, 2003.

[38] V. L. Marrero, J. A. Tichy, O. Sahni, and K. E. Jansen. Numerical study of purely viscous non-Newtonian flow in an abdominal aortic aneurysm. *Journal of Biomechanical Engineering*, 136(10):101001, 2014.

[39] K. L. McIlhany and S. Wiggins. Eulerian indicators under continuously varying conditions. *Physics of Fluids (1994-present)*, 24(7):073601, 2012.

[40] W. Meng, F. Yu, H. Chen, J. Zhang, E. Zhang, K. Dian, and Y. Shi. Concentration polarization of high-density lipoprotein and its relation with shear stress in an in vitro model. *BioMed Research International*, 2009:695838–695838, 2009.

[41] C. Menichini and X. Y. Xu. Mathematical modeling of thrombus formation in idealized models of aortic dissection: initial findings and potential applications. *Journal of Mathematical Biology*, 73(5):1205–1226, 2016.

[42] K. P. Papadopoulos, M. Gavaises, and C. Atkin. A simplified mathematical model for thrombin generation. *Medical Engineering & Physics*, 36(2):196–204, 2014.

[43] T. W. Peach, M. Ngoepe, K. Spranger, D. Zajarias-Fainsod, and Y. Ventikos. Personalizing flow-diverter intervention for cerebral aneurysms: from computational hemodynamics to biochemical modeling. *International Journal for Numerical Methods in Biomedical Engineering*, 30(11):1387–1407, 2014.

[44] V. Peiffer, S. J. Sherwin, and P. D. Weinberg. Does low and oscillatory wall shear stress correlate spatially with early atherosclerosis? a systematic review. *Cardiovascular Research*, page cvt044, 2013.

[45] A. M. Plata, S. J. Sherwin, and R. Krams. Endothelial nitric oxide production and transport in flow chambers: the importance of convection. *Annals of Biomedical Engineering*, 38(9):2805–2816, 2010.

[46] C. Poelma, P. N. Watton, and Y. Ventikos. Transitional flow in aneurysms and the computation of haemodynamic parameters. *Journal of The Royal Society Interface*, 12(105):20141394, 2015.

[47] C. J. Schwartz, A. J. Valente, E. A. Sprague, J. L. Kelley, and R. M. Nerem. The pathogenesis of atherosclerosis: an overview. *Clinical Cardiology*, 14(S1):1–16, 1991.

[48] D. Sengupta, A. M. Kahn, J. C. Burns, S. Sankaran, S. C. Shadden, and A. L. Marsden. Image-based modeling of hemodynamics in coronary artery aneurysms caused by kawasaki disease. *Biomechanics and Modeling in Mechanobiology*, 11(6):915–932, 2012.

[49] J. H. Seo, T. Abd, R. T. George, and R. Mittal. A coupled chemo-fluidic computational model for thrombogenesis in infarcted left ventricles. *American Journal of Physiology-Heart and Circulatory Physiology*, page 00855, 2016. `http://dx.doi.org/10.1152/ajpheart.00855.2015`.

[50] S. C. Shadden and A. Arzani. Lagrangian postprocessing of computational hemodynamics. *Annals of Biomedical Engineering*, 43(1):41–58, 2015.

[51] S. C. Shadden and C. A. Taylor. Characterization of coherent structures in the cardiovascular system. *Annals of Biomedical Engineering*, 36:1152–1162, 2008.

[52] E. N. Sorensen, G. W. Burgreen, W. R. Wagner, and J. F. Antaki. Computational simulation of platelet deposition and activation: I. model development and properties. *Annals of Biomedical Engineering*, 27(4):436–448, 1999.

[53] J. M. Tarbell. Mass transport in arteries and the localization of atherosclerosis. *Annual Review of Biomedical Engineering*, 5(1):79–118, 2003.

[54] J. Tong and G. A Holzapfel. Structure, mechanics, and histology of intraluminal thrombi in abdominal aortic aneurysms. *Annals of Biomedical Engineering*, 43(7):1488–1501, 2015.

[55] X. Tricoche, G. Scheuermann, and H. Hagen. Continuous topology simplification of planar vector fields. In *Proceedings of the conference on Visualization'01*, pages 159–166, 2001.

[56] P. E. Vincent and P. D. Weinberg. Flow-dependent concentration polarization and the endothelial glycocalyx layer: multi-scale aspects of arterial mass transport and their implications for atherosclerosis. *Biomechanics and Modeling in Mechanobiology*, 13(2):313–326, 2014.

[57] J. S. Wilson, L. Virag, P. Di Achille, I. Karšaj, and J. D. Humphrey. Biochemomechanics of intraluminal thrombus in abdominal aortic aneurysms. *Journal of Biomechanical Engineering*, 135(2):021011, 2013.

[58] E. Zhang, K. Mischaikow, and G. Turk. Vector field design on surfaces. *ACM Transactions on Graphics (TOG)*, 25(4):1294–1326, 2006.

List of Tables

List of Figures

Table 1: Point-wise Spearman's rank correlation coefficient between surface concentration and the different WSS parameters, relative residence time (RRT), WSS exposure time (WSSET), and WSS divergence (WSSdiv). The δn value used in WSSET calculations are different in each case. The correlation coefficient shown is the mean correlation coefficient between the different patients for the abdominal aortic aneurysm (AAA) and carotid patients. The 95% confidence intervals are shown in brackets. The confidence interval shown for AAA and carotid patients is the minimum lower bound and the maximum upper bound across all the patients.

	RRT	WSSET	WSSdiv
AAA patients	0.51 ± 0.09 [0.39,0.63]	0.79 ± 0.07 [0.70,0.87]	-0.47 ± 0.09 [-0.65,-0.36]
Carotid patients	0.84 ± 0.09 [0.77,0.91]	0.96 ± 0.01 [0.96,0.97]	-0.24 ± 0.04 [-0.29,-0.19]
Cerebral aneurysm	0.43 [0.41,0.44]	0.83 [0.82.0.83]	-0.57 [-0.58,-0.55]
Coronary aneurysm	0.82 [0.82,0.83]	0.87 [0.87,0.88]	0.02 [0.00,0.04]

Table 2: Percentage of the length of WSS unstable manifolds in the region greater than the 80th percentile of the WSS exposure time (WSSET) and surface concentration. The percentage shown is the mean percentage between the different patients for the abdominal aortic aneurysm (AAA) and carotid patients.

	WSSET	concentration
AAA patients	93.9 ± 5.0	79.2 ± 10.0
Carotid patients	97.7 ± 1.7	97.9 ± 0.5
Cerebral aneurysm	99.2	98.1
Coronary aneurysm	99.5	81.0
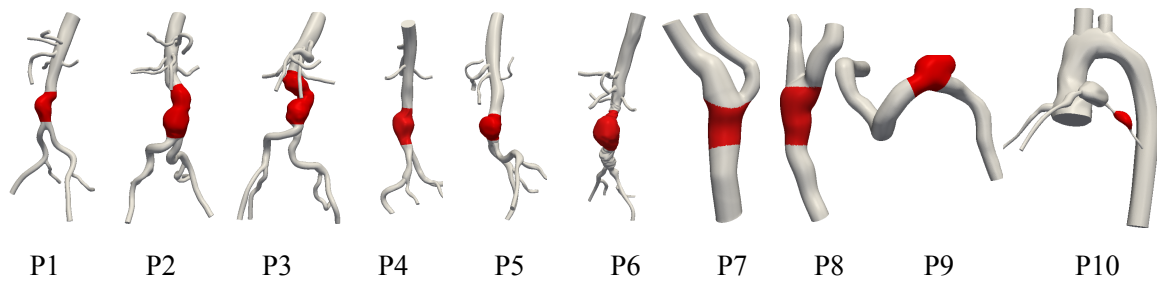
Figure 1: The full computational models where image-based CFD was performed. The highlighted region shows the region of interest where post-processing was performed. P1–P6 are the abdominal aortic aneurysm (AAA) models, P7–P8 are carotid artery models, P9 is a cerebral aneurysm model, and P10 is a coronary aneurysm model.
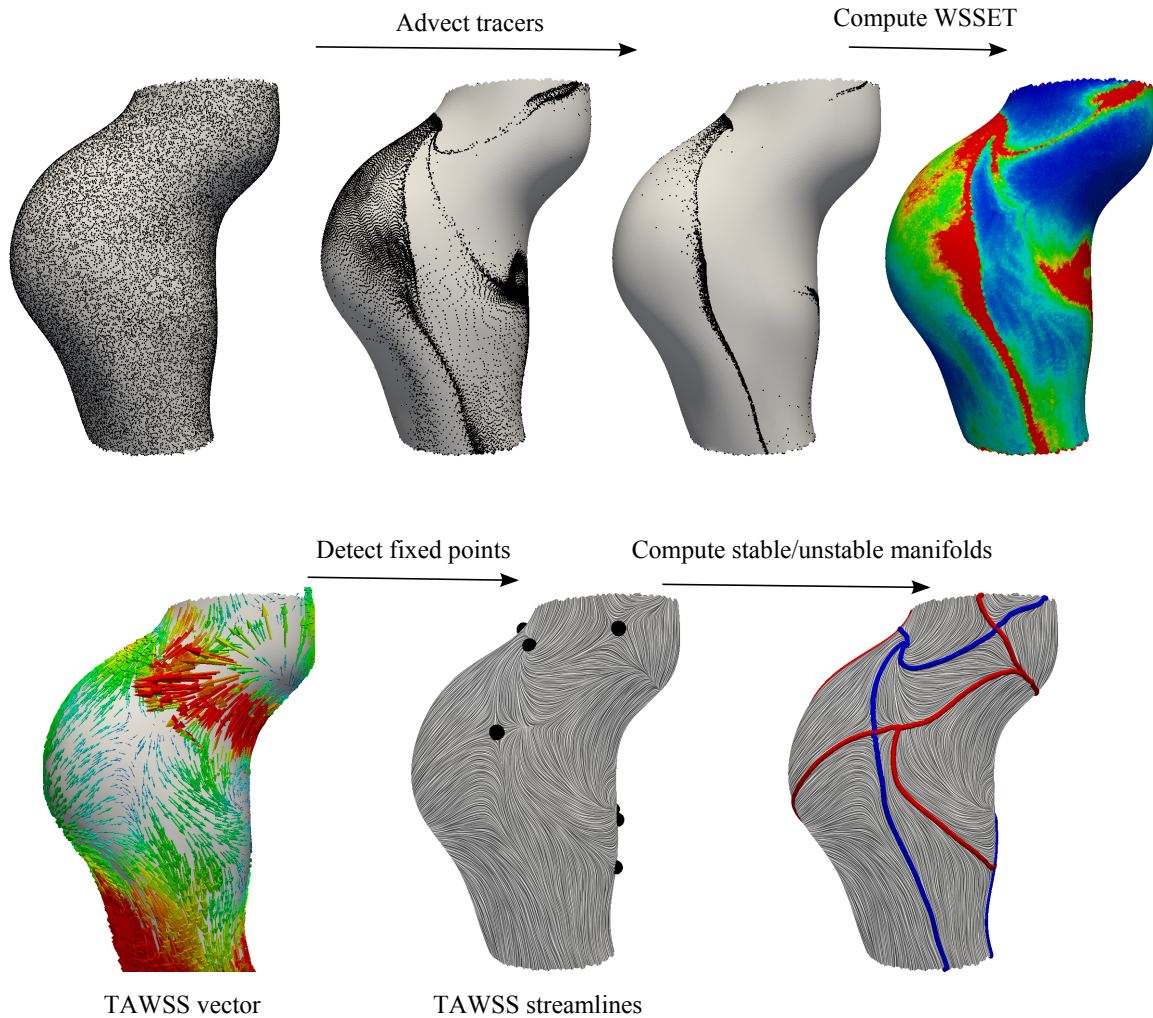
Figure 2: The procedure used in computation of WSS exposure time (WSSET) and TAWSS stable (red lines) and unstable (blue lines) manifolds. Trajectories are seeded on the aneurysm surface and advected in forward time to compute WSSET. Stable and unstable manifolds of the TAWSS vector field corresponding to saddle-type fixed points are computed with backward and forward time integration, respectively. These manifolds usually terminate in fixed points of other types (e.g., source or sink).
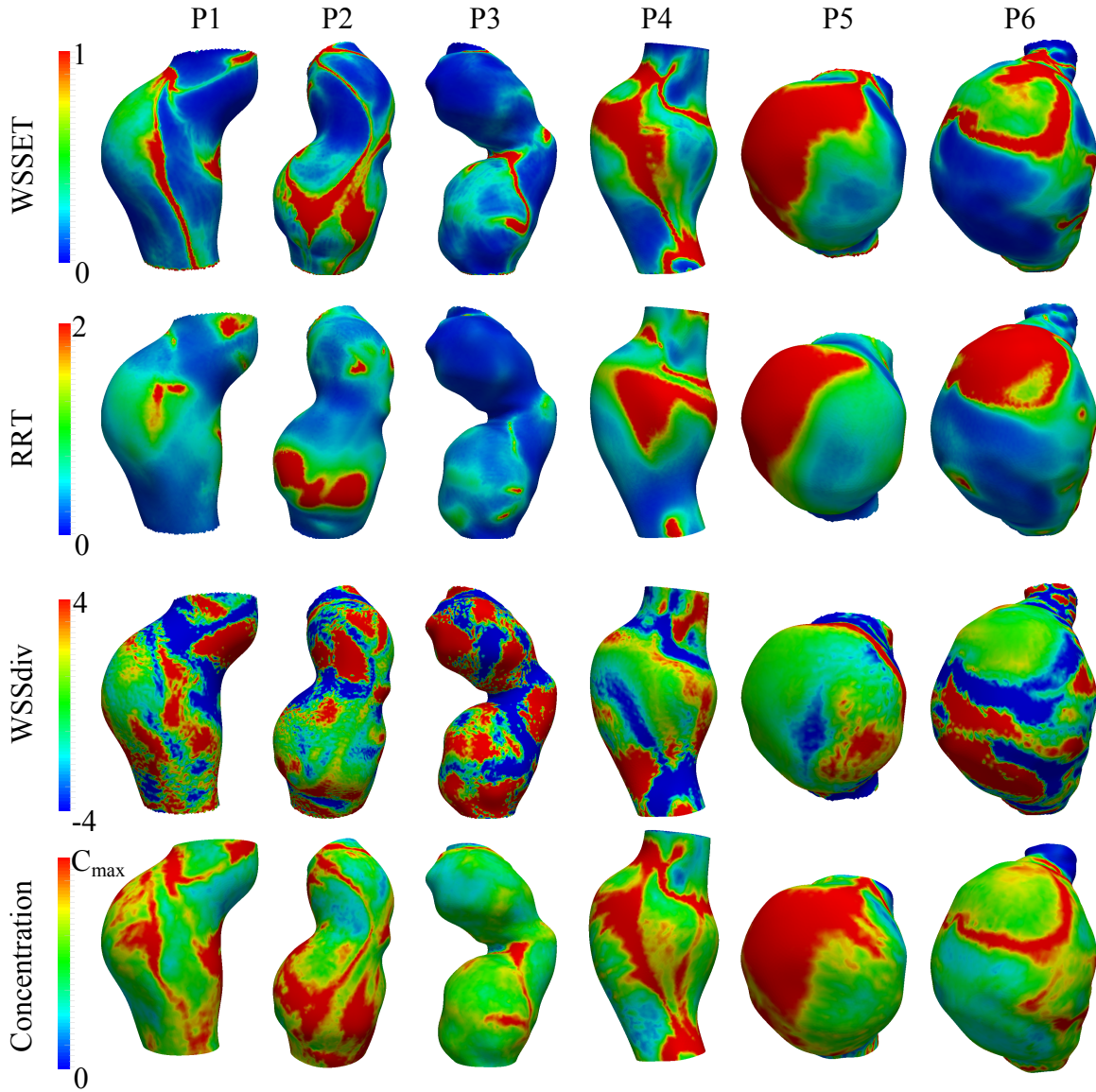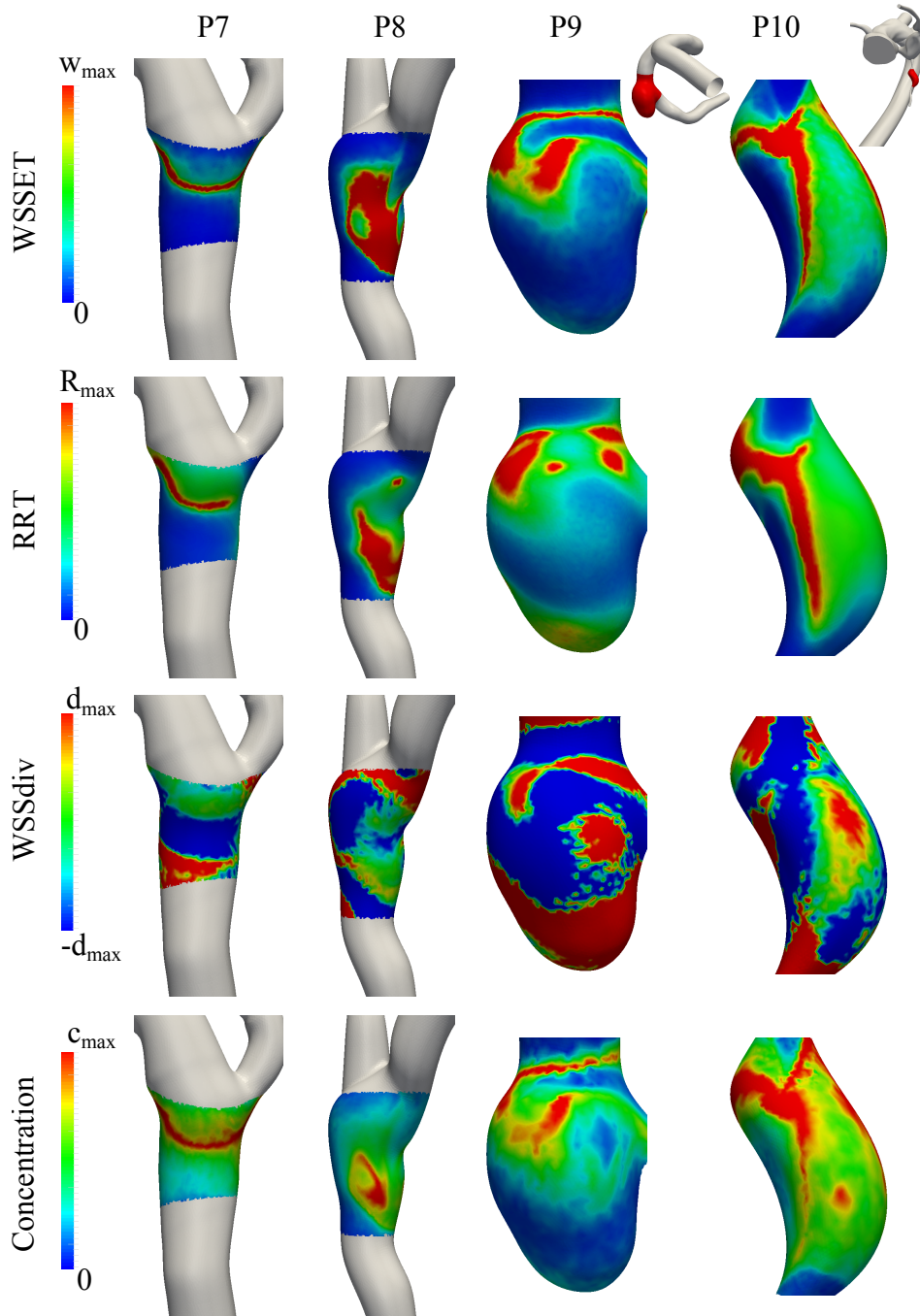
Figure 3: Contour plots of WSS exposure time (WSSET), relative residence time (RRT), WSS divergence (WSSdiv), and surface concentration for the six abdominal aortic aneurysm patients. RRT and WSSdiv units are $\frac{cm^2}{dynes}$ and $\frac{dynes}{cm^3}$, respectively. WSSET and concentration are defined dimensionless. Th C_{max} value in the colorbar is equal to 0.08 for Patient 1, 2, 4, and 5. It is equal to 0.03 and 0.04 for Patient 3 and 6, respectively. Same view as Figure 1 is shown.

Figure 4: Contour plots of WSS exposure time (WSSET), relative residence time (RRT), WSS divergence (WSSdiv), and surface concentration for the carotid (P7–P8), cerebral aneurysm (P9), and coronary aneurysm (P10) patients. RRT and WSSdiv units are $\frac{cm^2}{dynes}$ and $\frac{dynes}{cm^3}$, respectively. WSSET and concentration are defined dimensionless. Th w_{max} value in the colorbar is equal to 2 for Patient 10 and 1 for the rest of the patients. R_{max} is equal to 1.5 for P7–P8, 0.3 for P9, and 0.5 for P10. d_{max} is equal to 10 for P7–P8 and 20 for P9–P10. c_{max} is equal to 0.04 for P10 and 0.05 for the other patients.
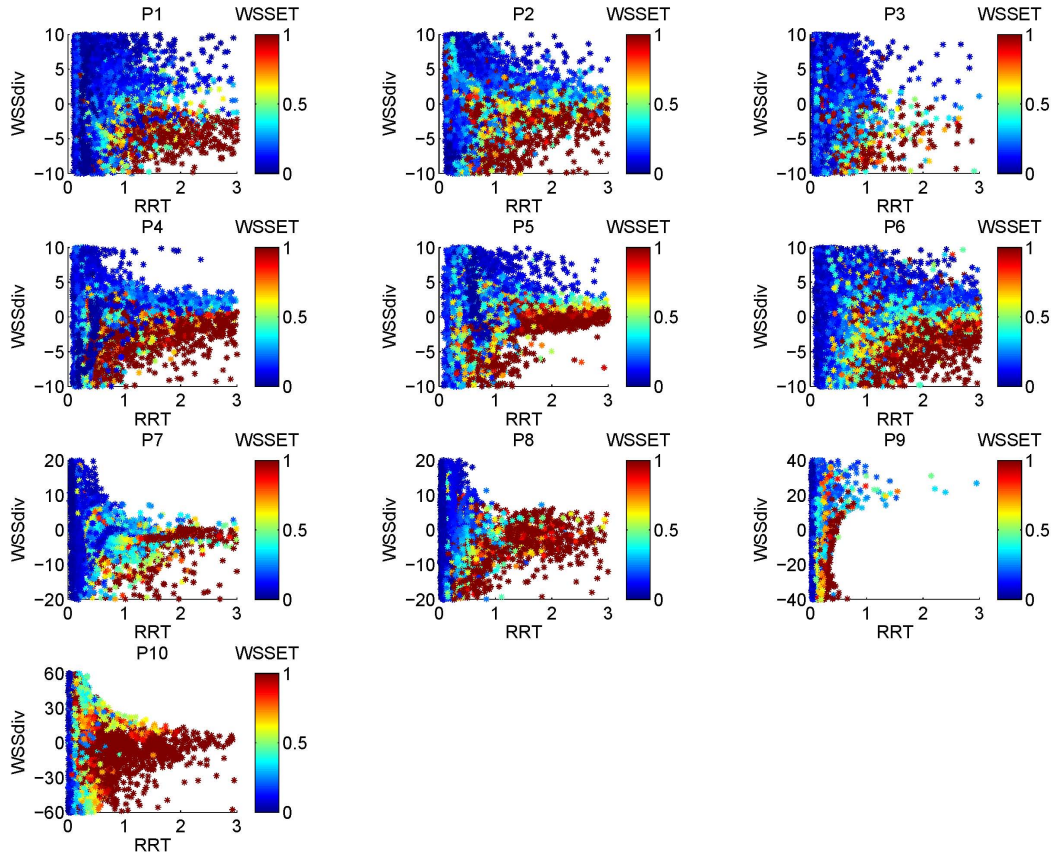
Figure 5: Scatter plots of WSS divergence (WSSdiv) vs. relative residence time (RRT), colored with the WSS exposure time (WSSET) value for all the patients. High WSSET occurs mostly in regions of high RRT and negative WSSdiv. RRT and WSSdiv units are $\frac{cm^2}{dynes}$ and $\frac{dynes}{cm^3}$, respectively. WSSET is defined dimensionless.
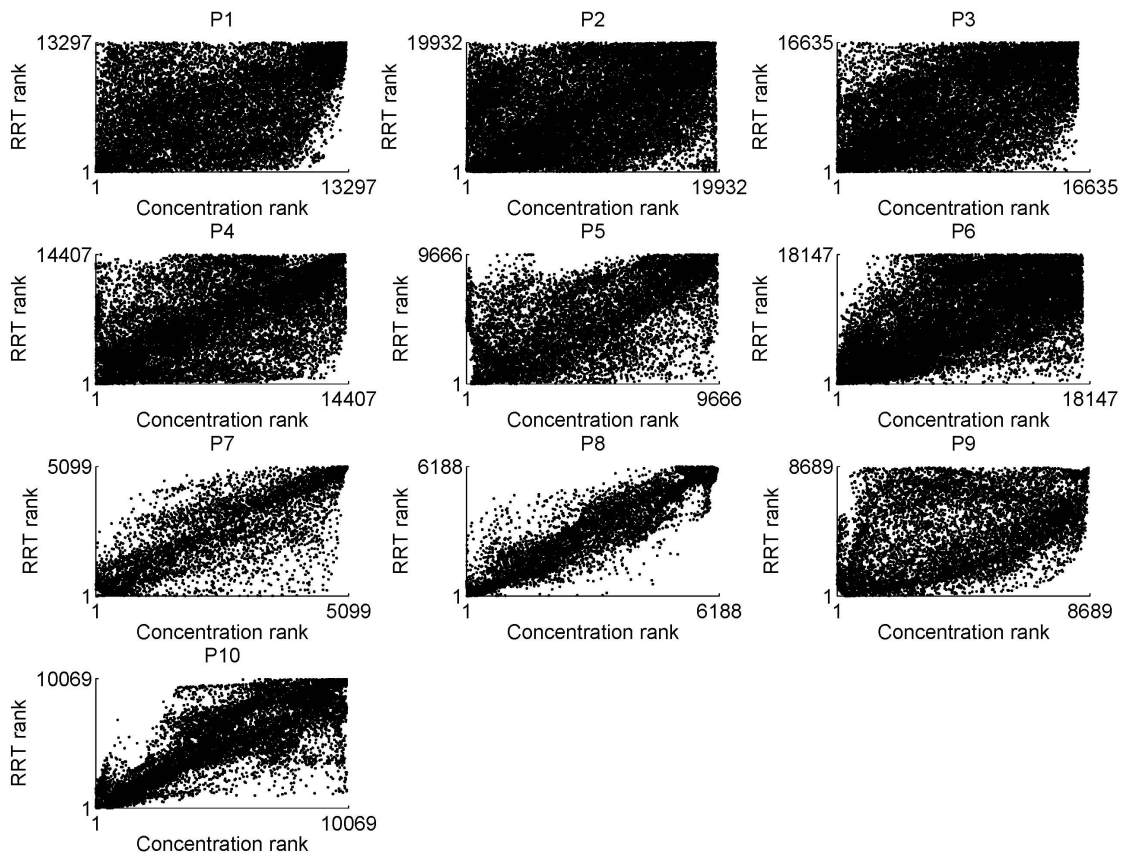
Figure 6: Scatter plots of relative residence time (RRT) rank vs. surface concentration rank for all the patients. Table 1 provides quantitative correlations based on these plots.
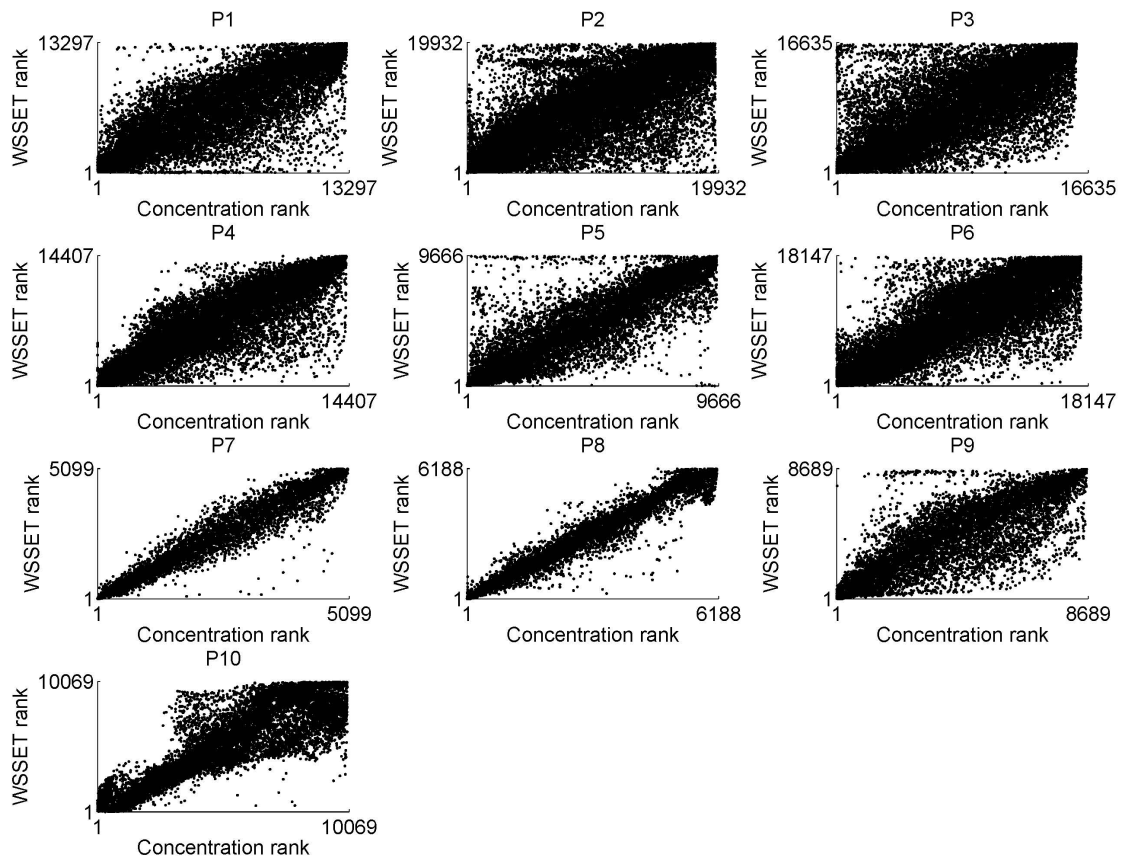
Figure 7: Scatter plots of WSS exposure time (WSSET) rank vs. surface concentration rank for all the patients. Table 1 provides quantitative correlations based on these plots.
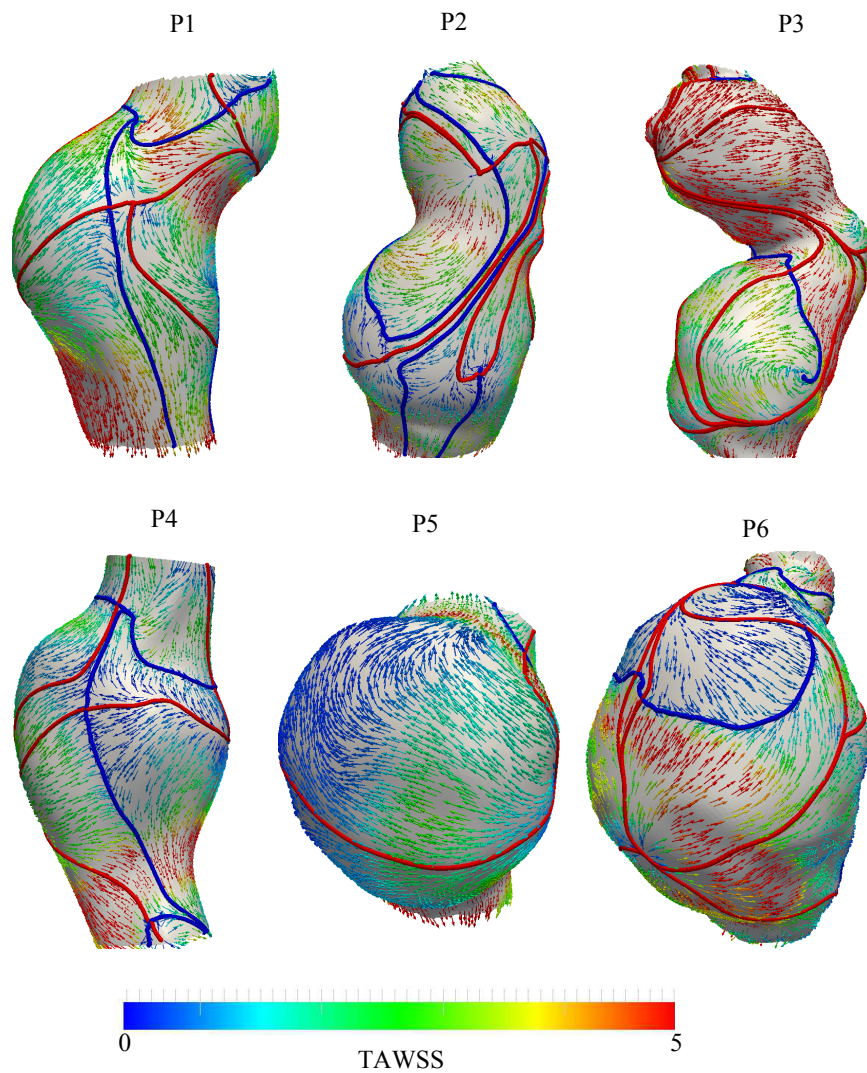
Figure 8: Stable (red line) and unstable (blue line) manifolds of TAWSS vector field for the six abdominal aortic aneurysm patients. The TAWSS vector length is normalized for visualization, and colored based on its magnitude. The unit for TAWSS is $\frac{dynes}{cm^2}$. Same view as Figure 3 is shown.
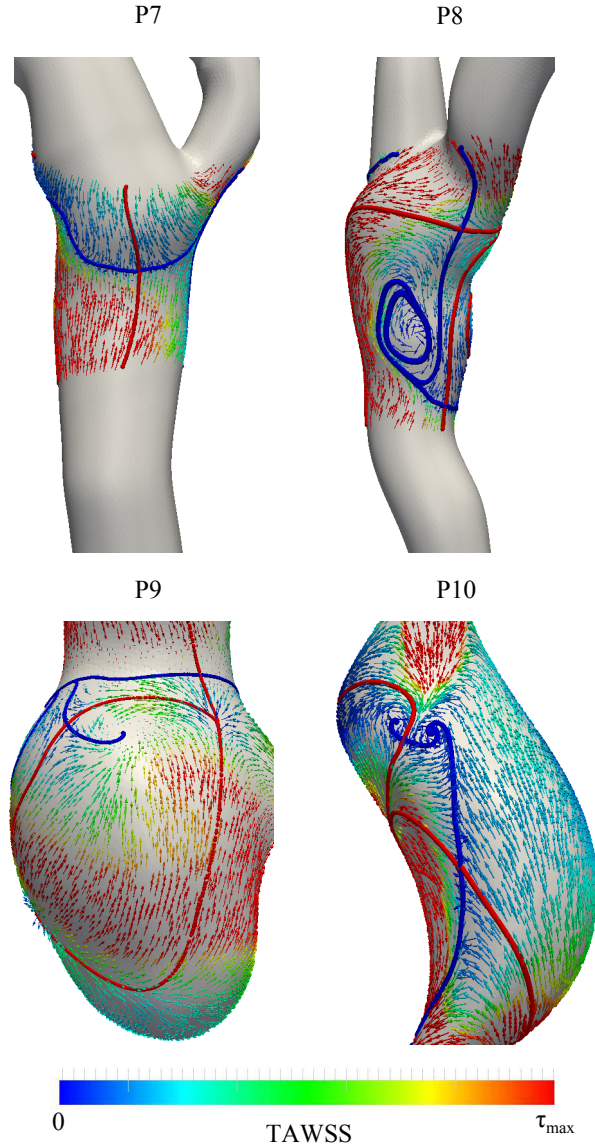
Figure 9: Stable (red line) and unstable (blue line) manifolds of TAWSS vector field for the carotid (P7–P8), cerebral aneurysm (P9), and coronary aneurysm (P10) patients. The TAWSS vector length is normalized for visualization, and colored based on its magnitude. The unit for TAWSS is $\frac{dynes}{cm^2}$. The τ_{max} value is equal to 10 for P7–P8 and 20 for P9–P10. Same view as Figure 4 is shown.
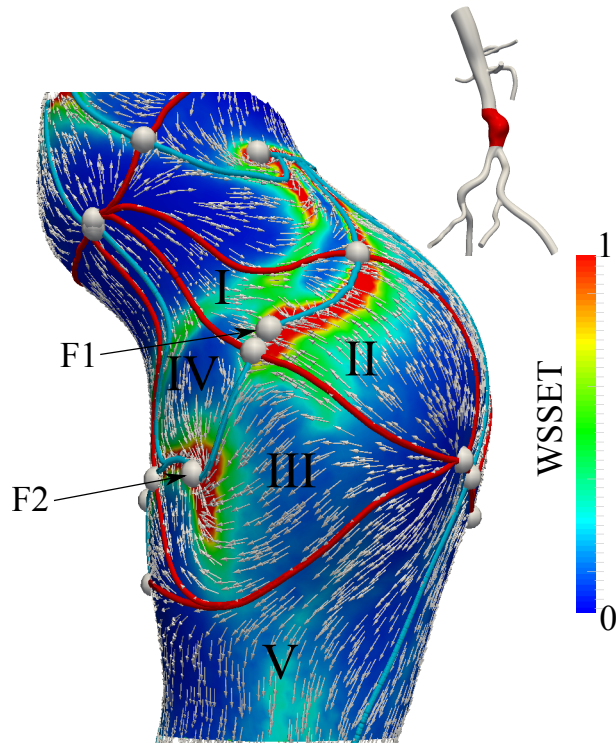
Figure 10: Intersection of stable (red line) and unstable (blue line) manifolds of the TAWSS vector divide the aneurysm surface into different regions. WSS trajectories in regions I and II are attracted to one TAWSS vector fixed point (F1), while trajectories in regions III and IV are attracted to another fixed point (F2). The TAWSS manifolds largely influence the WSS exposure time (WSSET). TAWSS vectors are normalized for visualization. Fixed points of TAWSS are marked with grey spheres. Patient 1 is shown in this figure.
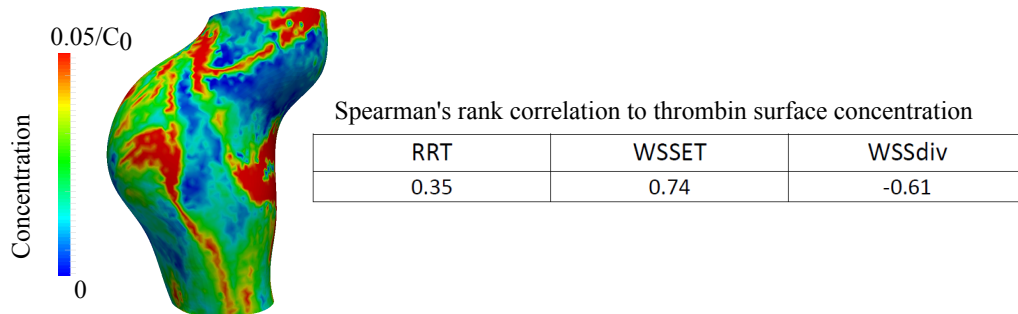

RRT	WSSET	WSSdiv
0.35	0.74	-0.61

Figure 11: Thrombin surface concentration normalized by the inlet prothrombin concentration (C_0). The point-wise Spearman's rank correlation coefficient between thrombin surface concentration and relative residence time (RRT), WSS exposure time (WSSET), and WSS divergence (WSSdiv) is also shown. Patient 1 is shown in this figure. Same view as Figure 3 is shown.